15.1 Observations and modeling of banded orographic conveciton

Daniel J. Kirshbaum and Dale R. Durran
University of Washington, Seattle, WA *

1. Introduction

Banded convection is a striking feature of the atmosphere that occurs in various different settings, including cloud "streets" in convective boundary layers, as well as squall lines and narrow frontal rainbands in midlatitude cyclones. Recent studies, among them Miniscloux et al (2001), Cosma et al (2002), Anquetin et al (2003), and Kirshbaum and Durran (2003), have suggested that well-defined convective bands may also develop in shallow orographic clouds. Miniscloux et al (2001) observed rainbands in two orographic rain events during the Cévannes experiment (1986-88) in France that continually formed over preferred locations, allowing for substantial localized rainfall enhancements. Motivated by these results, numerical studies by Cosma et al (2002) and Anquetin et al (2003) hypothesized a physical mechanism for such quasi-stationary rainbands involving the linear patterns of upward motion forced by flow over and around isolated peaks on the mountainous terrain. This mechanism, however, does not explain the parallel convective bands that developed in the numerical simulations of Kirshbaum and Durran (2003) over smooth mountain ridges. Rainbands produced in the 3D simulations of that study, which greatly increased precipitation over that produced by otherwise identical 2D simulations, were preferentially aligned with a zonal cross-barrier flow that increased linearly with height.

As a whole, the recent studies on orographic rainbands suggest that these features may be an important form of convection in some shallow orographic rain events because they have the potential to substantially enhance precipitation accumulations. However, the limited number of observational cases where these structures have been documented to exist, along with questions regarding the physical mechanisms behind their formation, have made it difficult to draw any firm conclusions regarding their frequency and dynamics. To further our understanding of orographic rainbands, three recent cases of shallow orographic convection exhibiting varying levels of bandedness over the Coastal Range in western Oregon are presented in this investigation, along with numerical simulations of these events and brief discussions of the differences between the convective behavior observed in each case.

The regional topography of western Washington and northwestern Oregon, as shown in Fig. 1, is characterized by two essentially parallel north-south oriented mountain ranges. The Olympics in Washington state and the Coastal Range in Oregon together comprise the western flank, which is much lower and narrower than the Cascade range to the east. A closer view of one section of the Coastal Range, bounded by latitudes of $45°$ N and $46°$ N and longitudes of $122.75°$ W and $124.25°$ W, is shown in Fig. 1. Operational radar data indicate that convective bands often form in orographic precipitation events over this elongated-ridge-like topography. In this study we analyze observations and perform numerical simulations of three cases of post-frontal orographic precipitation over this region. Radar observations and available rain gauge data obtained during these three events are presented and compared in section 2. Section 3 describes the estimation of upstream soundings for these events, which are used as inputs for the quasi-idealized numerical simulations described in section 4. The effects of small-scale surface topography on the observed and simulated orographic rainbands is discussed section 5, followed by a brief analysis of environmental parameters affecting the band formation in section 6. Concluding remarks are given in section 7.

2. Observations of banded convection

2.1 *Overview*

We now describe three convective precipitation events that occurred over the Oregon Coastal Range on 9-10 April 2002, 12-13 November 2002, and 12 October 2003, and are henceforth termed Case 1, Case 2, and Case 3, respectively. All three cases developed in similar synoptic settings, following the passage of mature surface cold fronts that had traveled for great distances over the Pacific Ocean. Due to their prolonged exposure to relatively warm ocean waters, the post-frontal air masses were warmed and moistened near the surface. By the time they made landfall on the west coast of North America, these air masses had developed considerable amounts of potential instability in the layer between the surface to about 700 mb. Shallow clouds and convective precipitation were produced as the potentially unstable air was lifted over the Coastal Range.

The convective organization in the three precipitation events under consideration is shown in Fig. 2 by $0.5°$ elevation radar images from the Portland, OR NEXRAD site, which has a nominal horizontal resolution of 1 km and is located approximately 60 km northeast of the center of the Coastal Range at an elevation of 541 m above sea

**Corresponding author address:* Daniel Kirshbaum, Department of Atmospheric Sciences, University of Washington, Seattle, WA 98107; e-mail: dank@atmos.washington.edu

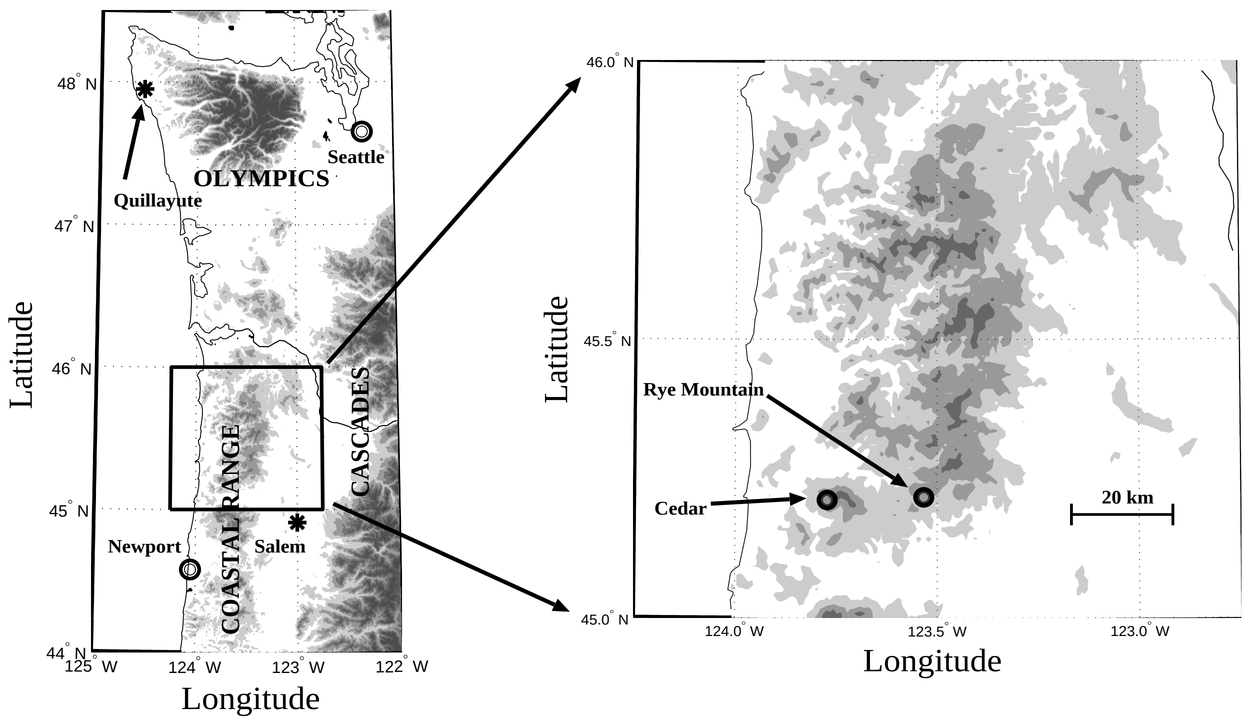

FIG. 1: Topography of Pacific Northwest United States and Coastal Range, shown at 250 m intervals. Circles indicate locations of surface data stations, asterisks denote radiosonde sites.

level. To more clearly show the relationship between the precipitation and the underlying topography, contours of radar reflectivity data, smoothed by a nine-point spatial filter, are overlaid upon shaded 250 m contours of the topography. Two images for each case are presented approximately one hour apart to illustrate the time evolution of convective rainfall during these events. The precipitation exhibited varying degrees of organization, with Case 2 (Figs. 2c and 2d) clearly displaying the most organized and robust banded structures. More detailed comparisons of the radar observations for these three events will be presented in the following.

2.2 *Radar observations*

The precipitating structures in Case 1, which developed after the passage of a surface cold front at approximately 2200 UTC on 9 April 2002 and continued for over five hours, are apparent from the contoured radar images at 2316 UTC on 9 April 2002 and 0017 UTC on 10 April 2002 respectively shown in Figs. 2a and 2b. Observed rainfall areas over the Coastal Range varied in structure from disorganized cells (Fig. 2a) to linearly-oriented bands (Fig. 2b). Rainbands such as those seen in Fig. 2b developed repeatedly over the elevated terrain from 2330 UTC to 0240 UTC, propagating downstream with the flow once initiated. After advecting into the lee of the Coastal Range, the bands were replaced by fresh convection on the upslope, in some cases forming over nearly identical locations as the departing structures. While the locations of bands B1 and B2 directly downstream of isolated small-scale peaks in Fig. 2b suggest that these structures may be fixed to topographic obstacles, other bands (e.g., B3) were not associated with obvious features on the terrain.

During Case 2, well-defined banded structures formed in post-frontal flow over the Coastal Range at approximately 1800 UTC on 12 November 2002 and persisted for seven hours in a quasi-stationary pattern. The remarkable steadiness of the convective bands in this event is indicated by the similarities between contoured radar plots at 2003 UTC and 2102 UTC on 12 Nov. 2002 in Figs. 2c and 2d, respectively. Note that the locations of rainbands labeled B4, B5, and B6 in Fig. 2c are nearly identical one hour later (Fig. 2d); these bands persisted in similar locations throughout this entire precipitation event. As in Case 1, some of the bands (e.g., B4 and B5) were located above or downstream of isolated topographic peaks, while others (e.g., B6) could not be clearly tied to small-scale terrain features. The intensity and stationarity of the rainbands in this case resulted in dramatic small-scale variability in the seven-hour cumulative precipitation. For example, the observation sites of Cedar and Rye Mountain, which are shown in Fig. 1 to lie about 20 km apart in the east-west direction, recorded vastly different amounts of rainfall. Cedar, positioned directly under precipitation band B4, recorded a maximum hourly rainfall accumulation of 19 mm and seven-hour accumulation of 69 mm, while Rye Mountain received only 3 mm of total precipitation. By contrast, precipitation accumulations were very light (less than 9 mm) and did not vary significantly between these same two locations in Cases 1 and 3.

Case 3 occurred in post-frontal flow over the Coastal Range from 1500 to 2300 UTC on 12 Oct. 2003, and was characterized by more disorganized precipitation patterns than in the previous two cases. Radar reflectivities at 1856 and 2000 UTC on 12 Oct. 2003 (Figs. 2e and 2f, respectively) indicate small-scale banded structures (e.g., B7 and B8 in Fig. 2f) forced by the mountainous terrain, along with more cellular precipitation areas (e.g., C1) that formed primarily in the flow upstream of the Coastal Range and intensified while advecting eastward over the elevated terrain. Although some rainbands, such as B7 and B8, formed in the vicinity of small-scale topographic peaks as in Cases 1 and 2, they were much less elongated and lasted for comparatively shorter periods than the orographic bands in the previous cases. As a result, the maximum precipitation accumulations recorded in Case 3 (8 mm at Rye Mountain) were far less than those in Case 2 (69 mm at Cedar) despite the comparable radar reflectivities and precipitation coverage apparent between the two events in Fig. 2.

2.3 *Comparison of precipitation bands*

The radar reflectivity images in Fig. 2 show precipitating structures that varied substantially between Cases 1, 2, and 3. Because this radar data has been smoothed and contoured at 10 dBZ intervals, however, some of the more subtle features in the precipitation fields may not be evident. To more closely compare the properties of the precipitation bands in the three cases, grayscale images of raw radar data are provided for each case in Fig. 3. An example of the more accurate and detailed picture provided by the raw data is seen by comparing Fig. 2b and Fig. 3a, which correspond to the same observation time. While the smoothed contour plot in Fig. 2b clearly shows the presence of precipitation bands, their true spacing and fine-scale structure at that time can only be appreciated from the raw data in Fig. 3a.

Estimates of the mean orientation, width, and spacing of the convective bands, as well as maximum radar reflectivities of precipitation over the Coastal Range, are found from Fig. 3 and provided in Table 1. Mean spacings could only be determined for the well-organized precipitation bands of Cases 1 and 2; the bands in Case 3 were too isolated for a representative value to be estimated. The quasi-steady precipitation bands in Case 2 possessed the largest average band widths (4 km) and spacings (8 km), while the more disorganized convective structures in Case 3 had the highest maximum radar eflectivities (50 dBZ). Convective bands in Case 1, while well-organized over the mountainous terrain, had the lowest horizontal scales and weakest maximum reflectivities.

3. Upstream soundings

Vertical sounding profiles upstream of the Oregon Coastal Range serve two important purposes in this study: first, the basic-state atmospheric structures yield valuable insight into the dynamical behavior of the flows under consideration; second, these profiles function as inflow boundary conditions for the quasi-idealized numerical simulations to be discussed in section 4. The determination of soundings upstream of the Coastal Range, however, is complicated by the fact that this region lies over the open ocean, where no instrumentation exists to gather sounding data. A best-guess estimate of the upstream conditions is therefore created from soundings collected at Salem, OR (see Fig. 1) by adjusting the low-level wind and thermodynamic variables to account for Salem's location on the lee side of the Coastal Range.

3.1 *Thermodynamic profiles*

Table 2 compares low-level temperatures (T), relative humidities ($\mathcal{H}$), and equivalent potential temperatures at the four pacific northwest locations indicated in Fig. 1. These date give surface and 850 mb radiosonde data from Salem and Quillayute, WA, as well as surface measurements from Newport, OR and Seattle, WA. The best available times for radiosonde soundings in these cases are 00 UTC on 10 Apr. 2002 (Case 1), 00 UTC on 13 Nov. 2002 (Case 2), and 00 UTC 13 Oct. 2002 (Case 3). For consistency the surface measurements from Newport and Seattle are provided at the same times. According to Table 2, the surface relative humidities at the coastal locations (Newport and Quillayute) are very similar for all three cases and much larger than the values further inland (Salem and Seattle). These west to east gradients in near-surface relative humidities, however, are not reflected in the equivalent potential temperatures; surface θ_e values in Table 2 are similar between Salem and Newport, as well as between Quillayute and Seattle. The differences in relative humidity between coastal and inland locations apparent at low levels are considerably reduced at higher elevations, as evidenced by the comparatively similar 850 mb humidities at Quillayute and Salem in Table 2. In addition, the vertical gradients of θ_e between the surface and 850 mb are consistent between Salem and Quillayute, suggesting that the low-level θ_e profiles have similar structure on either side of the coastal mountains.

From the above comparison it may be concluded that radiosonde data at Salem, while providing accurate estimates of the θ_e values upstream of the Coastal Range, do not reflect the high values of relative humidity observed at coastal locations. Thus, to generate upstream soundings that better represent conditions in the upstream flow, we have replaced humidity values

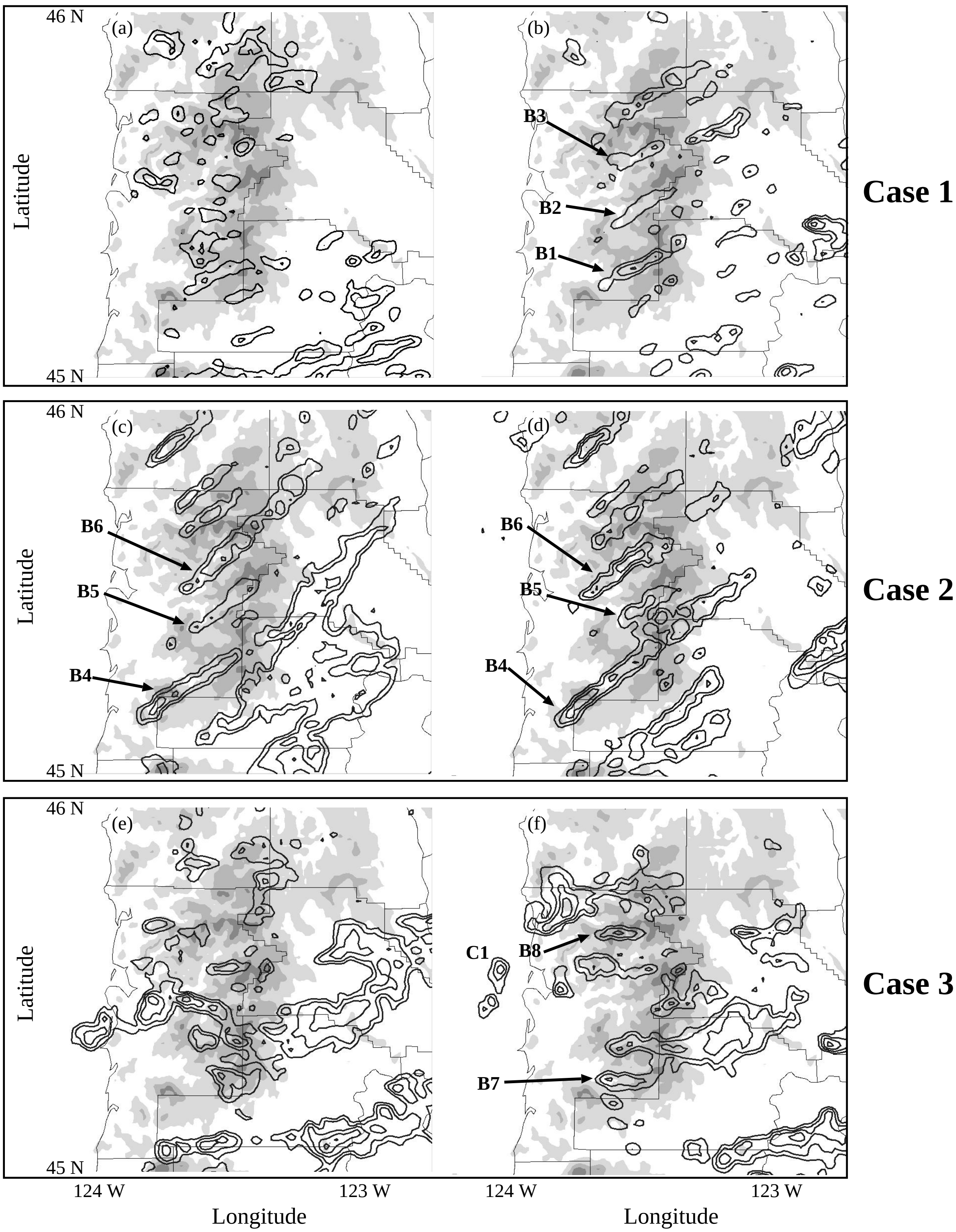

FIG. 2: Portland, OR NEXRAD images at 0.5° elevation for three cases of convective precipitation over Coastal Range topography. Case 1 at (a) 2316 UTC 9 Apr. 2002 and (b) 0017 UTC 10 Apr. 2002, Case 2 at (c) 2003 UTC 12 Nov. 2002 and (d) 2102 UTC 12 Nov. 2002, Case 3 at (e) 1856 UTC 12 Oct. 2003 and (f) 2000 UTC 12 Oct. 2003. Contour interval for grayscale topography is 250 m; contour interval for overlaid radar images is 10 dBZ.

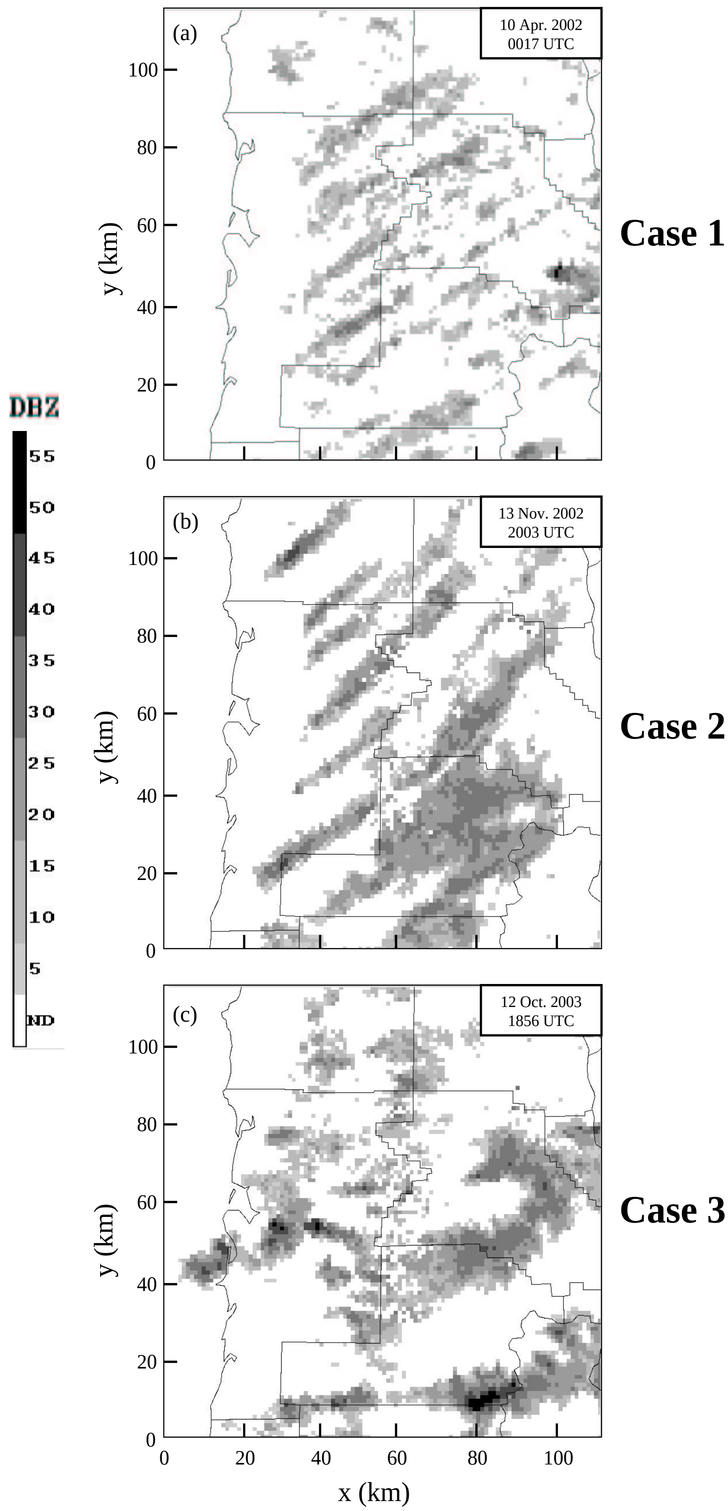

FIG. 3: Grayscale images of raw Portland, OR NEXRAD 0.5° elevation data for (a) Case 1, 0017 UTC 10 Apr. 2002, (b) Case 2, 2003 UTC 12 Nov. 2002, (c) Case 3, 1856 UTC 12 Oct. 2003.

Table 1: Comparison of precipitation properties for observed data and simulations of three precipitation events, measured from Figs. 3 and 7. Mean band alignment angle is measured counterclockwise relative to the east, mean width is defined as distance between 5 dBZ contours on the flanks of individual precipitation bands, mean spacing is distance between adjacent bands, and mean aspect ratio is quotient of horizontal lengths and widths of bands. For simulations, maximum reflectivity is calculated from simulated hydrometeor concentrations using Douglas (1964).

	Observed			Simulated		
Property	Case 1	Case 2	Case 3	Case 1	Case 2	Case 3
Alignment	$25-30°$	$30-35°$	$0-5°$	$20-25°$	$30-35°$	$0-5°$
Mean width (km)	2	4	2	2	3	3
Mean spacing (km)	4	8	N/A	3	5	N/A
Mean aspect ratio	6	6	2.5	7.5	7	3
Max. Ref. (dBZ)	30	35	50	35	45	50

from the Salem sounding in the surface to 850 mb layer with representative values from Quillayute (at identical times and linearly interpolated to represent the same elevations). A constant value of 90% was used over this layer for Cases 1 and 2, which was within 5% of the values measured at Quillayute, while values interpolated directly from the Quillayute sounding were used in Case 3 due to its comparatively large variations in humidity with height. An iterative procedure was then used to solve for the proper values of T and water vapor mixing ratio (q_v) necessary to maintain the θ_e profile observed in the Salem sounding. The raw thermodynamic data from Salem was left unchanged above the 850 mb level, resulting in the skew-T profiles shown in Figs. 4a, 4b, and 4c for Cases 1, 2, and 3, respectively. Profiles of θ_e and $\mathcal{H}$ for the three cases are also compared in Figs. 5a and 5b, showing that all three upstream soundings have potential instability from the surface to about $z = 2.5$ km and absolutely stable flow at higher levels. Likewise, the relative humidity profiles are similar for the three cases, with high values (greater than 80%) between the surface and $z = 2$ km and much lower values aloft.

3.2 *Velocity profiles*

Another field which undergoes significant modification as the flow approaches Salem from the Oregon coastline is the low-level velocity. Increased frictional dissipation over land heightens the surface stress and reduces the near-surface wind speeds as the flow moves inland. Due to the presence of the north-south oriented Coastal Range directly to the east, low-level flows at coastal stations may also be affected by upstream blocking and consequently cannot be assumed to accurately characterize the velocity in the undisturbed offshore flow. A rough estimate of the offshore conditions may, however, be inferred from short-term forecasts from numerical weather prediction models. Here we use 12 h forecasts from the Fifth-generation Pennsylvania State University-NCAR nonhydrostatic mesoscale model (MM5) to obtain predictions for surface velocities off the northwestern Oregon coast. These simulations were performed at the University of Washington over the Pacific northwest at 12 km horizontal resolution using boundary conditions from the National Center for Environmental Prediction GFS global model. MM5 predictions were combined with upper-level data from the Salem soundings to better represent upstream wind conditions in the three test cases. To smoothly connect the model and sounding data, the winds in the lowest kilometer are linearly interpolated between the MM5 surface values and the values observed at $z = 1$ km in the Salem soundings. The zonal flow (U) is westerly in all three cases and increases with height (Fig. 5c), whereas the meridional flow (V) exhibits considerable variability between the three events.

4. Quasi-idealized numerical simulations

To complement the observational data presented in section 2, numerical simulations have been performed that allow for more thorough examination of the physical mechanisms behind the observed behavior of shallow orographic convection. In this section we explore whether the precipitating structures seen in the radar data (Fig. 2) can be qualitatively captured in simulations. These experiments, while motivated by observed data, contain many idealizations and are hence termed “quasi-idealized” to reflect the fact that they should not expected to reproduce the exact structures, locations, and timing of observed precipitating features.

4.1 *Experimental setup*

The cloud-resolving, nonhydrostatic, fully nonlinear numerical model used in this study is described in Durran and Klemp (1983) and Epifanio and Durran (2001). This model contains a flux-limited scalar advection scheme (LeVeque 1996) to eliminate spurious overshoots caused by steep spatial gradients, a subgrid-scale turbulence formulation based on Lilly (1962), and a Kessler warm-rain parameterization for cloud microphysics. Ice processes are neglected for simplicity and because the cloud tops in these events generally did not extend far above the freezing level. Because of the relatively short cross-barrier extent ($\sim 50-100$ km) of the Coastal Range, the charac-

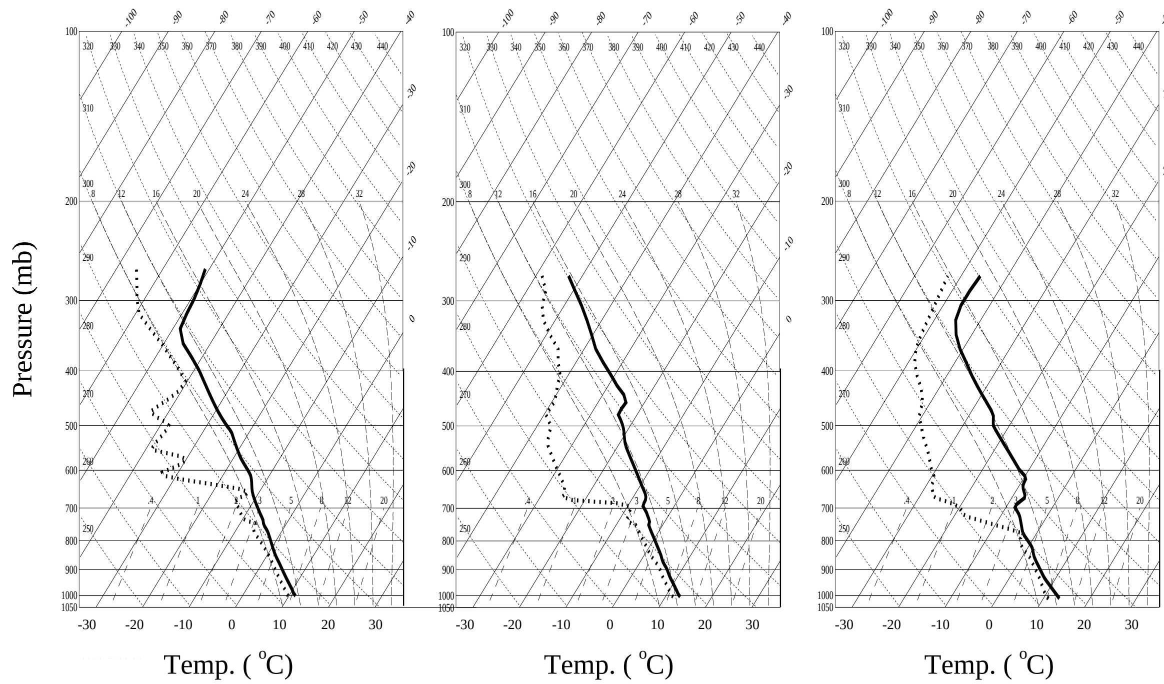

FIG. 4: Skew-T profiles for (a) Case 1, (b) Case 2, and (c) Case 3. Temperature profiles shown by solid line, dewpoint by dashed line.

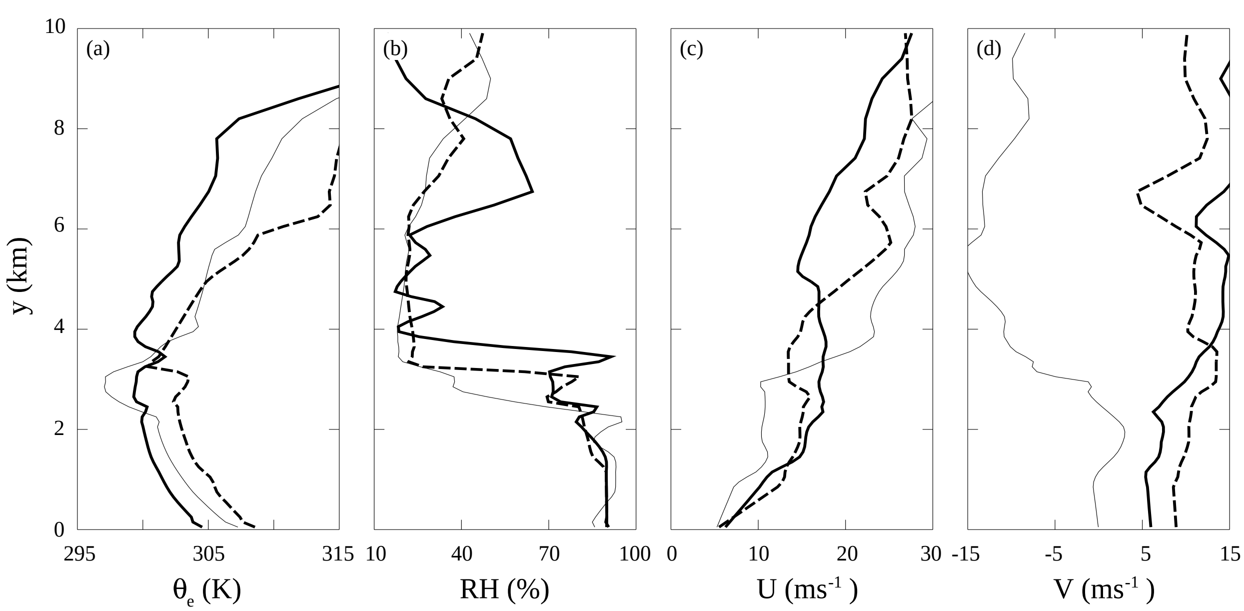

FIG. 5: Comparison of vertical profiles of (a) θ_e, (b) Relative humidity, (c) Zonal wind speed (U), and (d) Meridional wind speed (V) for three test cases. Case 1 given by thick solid line, Case 2 by thick dashed line, and Case 3 by thin solid line.

Table 2: Comparison of low-level thermodynamic data for three test cases: Temperature (T), Relative humidity ($\mathcal{H}$), and equivalent potential temperature (θ_e) provided at various locations and heights.

		Case 1 00 UTC 10 Apr. 2002			Case 2 00 UTC 13 Nov. 2002			Case 3 00 UTC 13 Oct. 2002		
Location	Height	T (K)	$\mathcal{H}$ (%)	θ_e (K)	T (K)	$\mathcal{H}$ (%)	θ_e (K)	T (K)	$\mathcal{H}$ (%)	θ_e (K)
Salem	surface	286.2	78	305.2	287.4	85	309.4	289.0	68	308.0
Quillayute	surface	283.0	100	303.1	285.0	90	306.1	286.2	88	307.0
Newport	surface	284.7	100	305.3	286.9	93	309.3	286.9	90	307.6
Seattle	surface	284.7	83	302.7	286.3	81	305.5	287.4	72	305.7
Salem	850 mb	277.8	92	300.8	278.8	87	304.7	286.2	80	301.9
Quillayute	850 mb	273.8	88	298.4	275.0	87	300.5	275.2	92	301.6

teristic Rossby numbers of these flows are large and rotational effects have consequently been neglected. The section of the Coastal Range highlighted in Fig. 1 is represented by an idealized finite-length ridge (h) of the following form

$$h(x,y) = \begin{cases} \frac{h_0}{16}\left[1+\cos(\pi r)\right]^4 & : \quad r \le 1 \\ 0 & : \quad \text{otherwise} \end{cases} \tag{1}$$

where

$$r^2 = \begin{cases} \left(\frac{x-x_0}{4a}\right)^2 + \left(\frac{|y-y_0|-B}{4b}\right)^2 & : \quad |y-y_0| > B \\ \left(\frac{x-x_0}{4a}\right)^2 & : \quad \text{otherwise} \end{cases} \tag{2}$$

In the preceding, $x_0 = y_0 = 225$ km, $h_0 = 1$ km, $a = 15$ km on the windward side of the mountain and 10 km on the lee, $b = 10$ km, and $B = 30$ km.

To provide high spatial resolution directly over the mountain while limiting the overall computational expense, three-level, two-way grid nesting has been employed. Figure 6 illustrates the grid configurations and terrain profile for these simulations, in which the outermost domain has dimensions of 450 km by 450 km, horizontal grid spacings (Δ) of 4.5 km, and an integration time step (Δt) of 36 s. Horizontal grid spacings are reduced to 1.5 km and 500 m on the two successively finer nested grids, with respective values of Δt reducing to 12 s and 4 s. The vertical resolution (Δz) is 100 m over $0 \le z < 5$ km, stretching linearly to 400 m over $5 \le z < 8$ km, then remaining constant at 400 m to the top of the domain at 10 km.

The vertical profiles shown in Fig. 4 are used as upstream boundary conditions for simulations of the three different test cases. As discussed in section 3, these profiles are intended to represent offshore conditions upstream of the Coastal Range, and may be expected to change significantly as the flows encounter greater frictional dissipation over land. To capture the effects of increased surface stress over land surfaces, frictional effects are included to the east of the idealized coastline, shown in Fig. 6 by the dashed line at $x = 165$ km. Surface friction is imposed in this region through a first-order Blackadar scheme based on Zhang and Anthes (1983) in which Monin-Obukhov similarity theory is assumed to prevail in a surface layer added to the model at $z = 10$ m. The large near-surface vertical shears forced by friction cause the Richardson number in that layer to fall below the critical value of 0.25 for dynamic instability, inducing subgrid-scale vertical mixing with adjacent layers and thereby deepening the shear layer with the passage of time. As the depth of this near-surface shear layer increases, the instability at its top eventually weakens to the point where continued upward growth of the boundary layer becomes negligible. In the simulations analyzed for this study, this quasi-steady state is generally reached after approximately three hours of integration time ($t = 10,800$ s) with boundary layer depths approaching 500-600 m.

To initiate convective motions within any statically unstable regions that develop in regions of saturated flow, small-amplitude random noise is added to the initial thermal field on the finest numerical grid (labeled grid 3 in Fig. 6), and at all subsequent time steps on the upstream boundaries of that grid. This noise field is created by assigning a uniformly distributed random number to each thermodynamic gridpoint, filtering these values by a single application of a diffusion operator along each coordinate axis to remove all forcing at 2Δ, and then scaling the field to have a 0.1 K root-mean-squared (rms) amplitude. A similar methodology is used to create small-amplitude irregularities on the mountainous topography; these small-scale surface bumps, which are filtered four times through a two-dimensional diffusion operator to remove topographic forcing at the model's least resolvable scales, are scaled to have an rms amplitude of 30 m. Note that this amplitude is only 3% of the maximum mountain height (1 km).

4.2 *Simulation results*

The convective structures produced by quasi-idealized numerical simulations of Cases 1, 2, and 3 are revealed by the horizontal cross-sections of the rainwater mixing ratio (q_r) displayed in Fig. 7. To allow for direct compari-

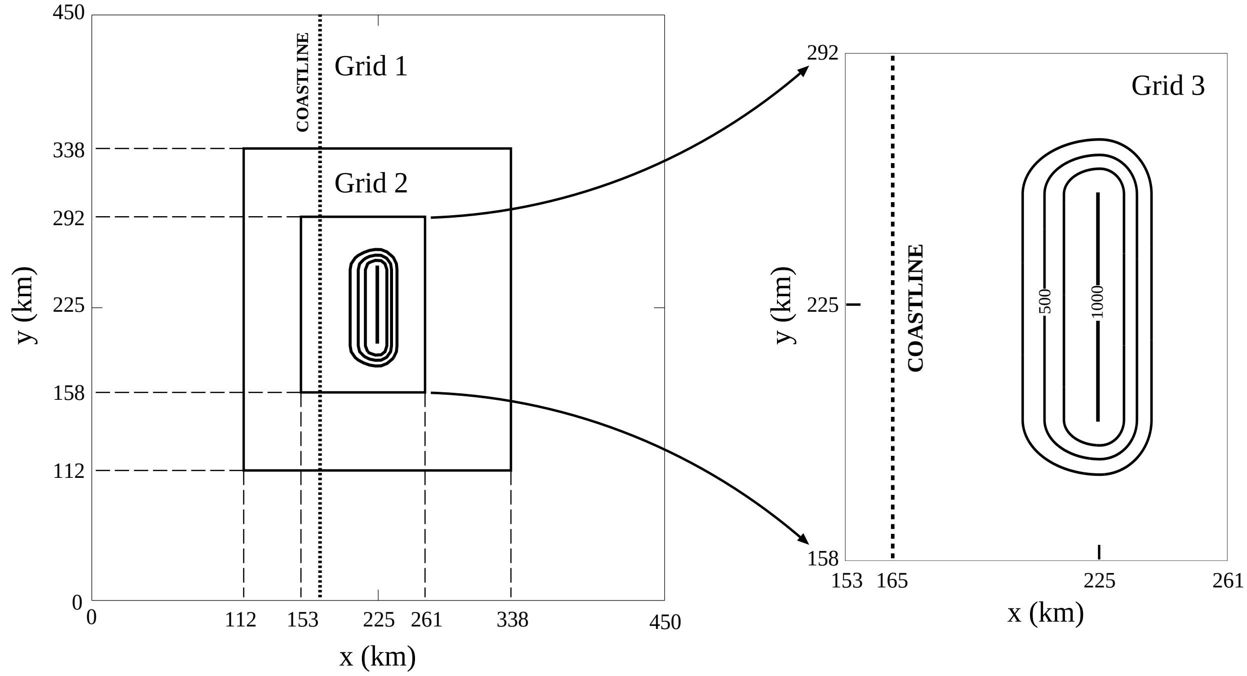

FIG. 6: Numerical domain for quasi-idealized simulations showing the grid nesting and contours of the topography at 250 m intervals.

son with the radar images in Fig. 2, the simulation results are provided at a height of $z = 1.2$ km, representative of the level reached by the $0.5°$ elevation Portland NEXRAD radar beam over the Coastal Range upslope, and at two integration times separated by one hour ($t = 4$ h and $t = 5$ h). By 4 h, the evolution of mesoscale processes such as boundary layer development and mountain wave formation are, to a good approximation, completed, allowing for examination of the dynamics of orographic clouds in a steady background environment. Cumulative surface precipitation at $t = 5$ h is also plotted in Fig. 7 to illustrate the integrated effect of the convective rainfall over the length of the simulation.

From inspection of Fig. 7 and Fig. 2, the simulated q_r fields in all three cases appear qualitatively similar to the rainfall patterns observed by the radar. Moreover, the basic variations between precipitating structures in the different events are reproduced by the numerical simulations. As in the radar data, the Case-2 simulation has the most stationary and well-defined bands. Their quasi-stationary character is apparent from the nearly identical locations of bands SB1, SB2, and SB3 in Figs. 7d and 7e, and from the banded appearance of the cumulative precipitation field in Fig. 7f. By contrast, the bands in Case 1 have lower intensities, slightly smaller horizontal scales, and reduced steadiness, as seen by the differences in the locations of the bands at $t = 4$ h and 5 h (Figs. 7a and 7b). While the cumulative precipitation field in Case 1 (Fig. 7c) exhibits a somewhat banded structure, the precipitation is much weaker and less localized than that of Case 2. Comparatively disorganized precipitating features are apparent in the Case-3 simulation (Figs. 7g and 7h); as in the radar observations, a combination of cellular and banded structures tend to develop upstream and over the mountainous topography. Some cells (e.g., SC1 and SC2 in Fig. 7h) form upstream of the mountain and strengthen while drifting over the elevated terrain, while other banded features such as SB4 in Fig. 7h develop directly over the mountain. The disorganized cells in Case 3 produce a broad region of light precipitation over the mountain (Fig. 7i) that is enhanced in certain locations where elongated rainbands like SB4 repeatedly develop.

The basic features of radar observations and simulated data for the three test cases are quantitatively compared in Table 1. In all cases, the horizontal alignment of convective bands is represented accurately by the numerical simulations, while the widths and spacings of the bands are slightly underestimated and maximum reflectivities slightly overestimated[1]. Convective bands also tend to be slightly more elongated in the simulations, as seen by the modest increases in mean aspect ratio for the three cases in Table 1. To a certain extent, this lack of complete quantitative agreement between observations and simulations is to be expected, considering the many approximations contained in the simulations. Nonetheless, the ability of numerical simulations to produce

[1]Radar reflectivities Z are calculated in simulations from q_r values through a conversion algorithm from Douglas (1964): $Z = 2.4 \times 10^4 M^{1.82}$, where $M = \rho_{dry} q_r$.

convective features with physically realistic structures and intensities—and qualitatively capture the basic differences apparent between observed cases—suggests that simulations may serve as a useful tool for evaluating the factors controlling the behavior of shallow orographic convection.

5. Influence of small-scale topography upon bandedness

The observations and numerical simulations presented herein have illustrated that banded structures of varied intensity, organization, and steadiness form in post-frontal shallow convective episodes over the Oregon Coastal Range. Rain gauge data over the upslope of this mountain range, while limited to only two sites, have shown that considerable local precipitation enhancements result when organized, quasi-stationary orographic rainbands dominate the precipitation pattern. Although a more thorough analysis of the physical factors affecting the structure and propagation of these rainbands will be deferred to a future investigation, some preliminary insight is now provided. In this section the influence of terrain roughness is considered; section 6 will evaluate environmental factors not directly related to the underlying topography.

5.1 *Comparison of smooth and roughened topographies*

We begin our investigation into the effects of small-scale topographic roughness upon orographic convection by comparing the three simulations just described in section 4 with three simulations that are identical except that no random noise was added to the topography, leaving just the smooth mountain profile given by (1). Inspection of horizontal cross sections of the q_r and cumulative precipitation fields indicates that convection in the smooth-mountain cases (Fig. 8) is generally similar in both structure and intensity to that produced in cases with roughened topography (Fig. 7). Nevertheless, systematic differences are apparent in those cases that develop well-defined orographic rainbands: Cases 1 and 2. In these cases, the bands are longer and more regularly spaced over the roughened terrain (Figs. 7a-7f) than over the smooth mountain (Figs. 8a-8f). In addition, the randomly distributed small-scale bumps strongly increase the overall steadiness of the orographic rainbands in Cases 1 and 2. Convective bands that form in the smooth topography simulations propagate downstream with the prevailing flow, continually being replaced by fresh convection in new locations on the upslope. Over roughened topography, on the other hand, rainbands such as SB1, SB2, and SB3 in Figs. 7d and 7e remain almost stationary for extended periods. The steadiness of the rainbands over the roughened terrain creates much more banded cumulative precipitation fields (Figs. 7c and 7f) with far larger precipitation maxima (15 mm and 43 mm, respectively) than the corresponding simulations with smooth terrain (Figs. 8c and 8f), in which the respective precipitation maxima are only 5 mm and 16 mm.

Compared with Cases 1 and 2, the differences between the convective formations in the smooth and roughened topography simulations of Case 3 are far less obvious. Although the rainbands that develop directly over the mountain (e.g., SB4 in Fig. 7h) are slightly more elongated and steadier over the roughened terrain than over smooth terrain, convective cells that form in the flow upstream of the mountain and propagate over the orography (e.g., SC1 and SC2) tend to be randomly distributed over the mountainous terrain and not strongly affected by small-scale terrain fluctuations. Because these cellular features dominate the rainfall pattern, the precipitation is distributed over much broader regions than that in Cases 1 and 2 regardless of the roughness of the underlying terrain. As a result, the addition of topographic roughness produces only a modest increase in maximum precipitation (29 mm in Fig. 7i) compared to the smooth mountain simulation (23 mm in Fig. 8i).

5.2 *Relationship between small-scale topographic features and band structure*

The preceding comparison of simulated flows over smooth and roughened mountains showed the importance of small-scale topographic irregularities in organizing convective orographic rainfall, particularly for the more banded events (Cases 1 and 2). Moreover, the radar data in Fig. 2 suggested that some of the observed rainbands preferentially formed downstream of isolated sub-range-scale peaks within the Coastal Range. The relationship between orographic rainbands and small-scale topography was previously investigated by Cosma et al (2002, hereafter denoted by CRM), who determined that the upward motions forced by ascent over and flow convergence downstream of isolated peaks on the mountainous terrain caused flow-parallel rainbands to develop in the lee of the obstacles. This conclusion was reached through analysis of observed precipitation events over the Cévannes region of France, as well as idealized simulations of moist flow over gradually-sloping topography representative of the region with superposed isolated large peaks of 1.2 km height and 10 km half-width. Similar experiments as those of CRM, carried out by adding isolated bumps 500 m high with 2.5 km half-widths to locations on the upslope of the smooth topography Case 2 simulation (not shown), have verified the basic result that convective rainbands may preferentially form over and downstream of small-scale topographic obstacles. The effects of the isolated peaks varied greatly depending on their location relative to the ridge crest, suggesting that only favorably-positioned peaks may be expected to have a sizeable impact on the precipitation distribution.

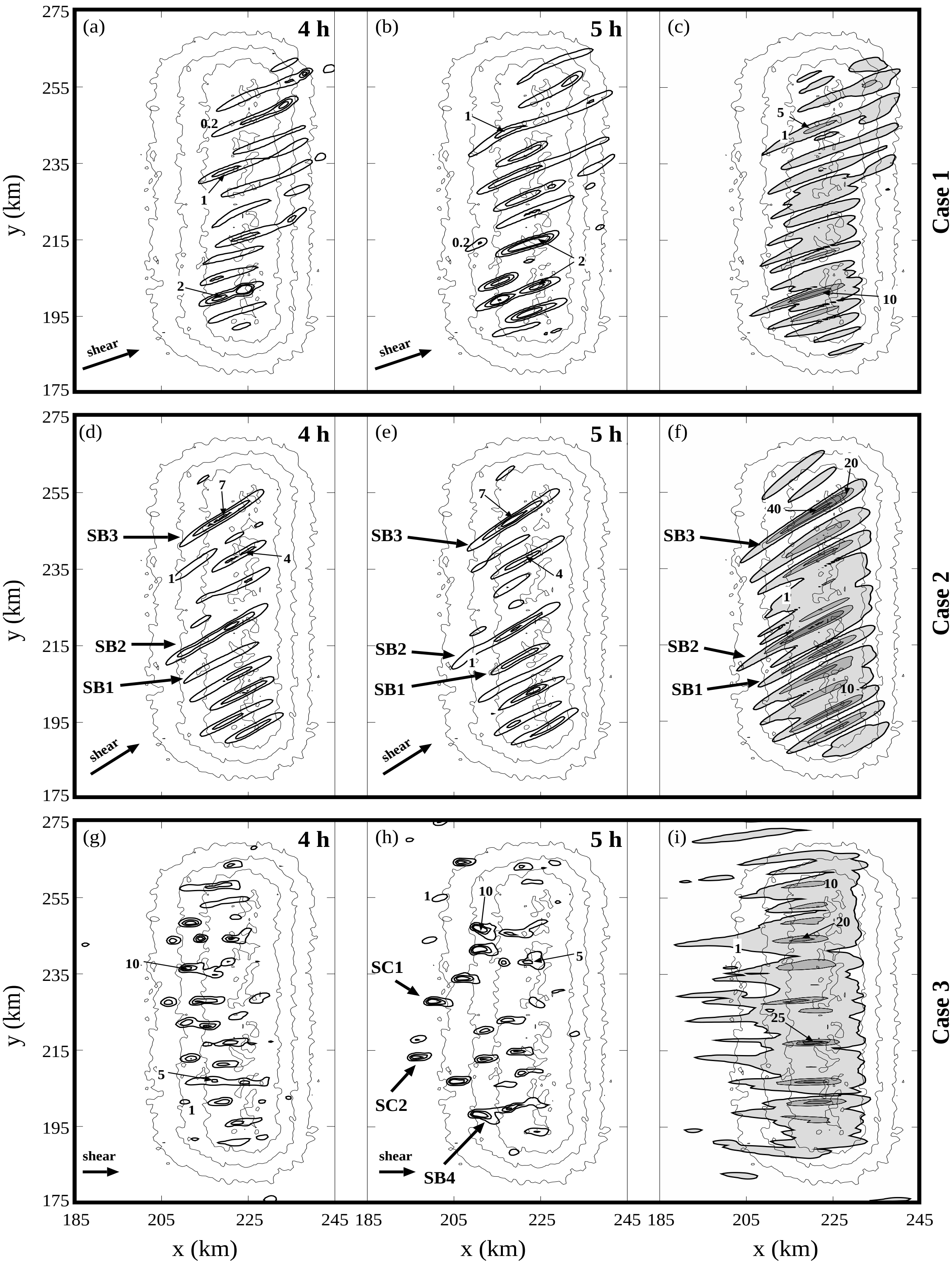

FIG. 7: Quasi-idealized simulation results over roughened topography. Case 1 rainwater mixing ratios (q_r) at (a) $t = 4$ h and (b) $t = 5$ h and (c) cumulative precipitation at $t = 5$ h; Case 2 q_r at (d) $t = 4$ h and (e) $t = 5$ h and (f) cumulative precipitation at $t = 5$ h; Case 3 q_r at (g) $t = 4$ h and (h) $t = 5$ h and (i) cumulative precipitation at $t = 5$ h. Arrows overlaid on q_r plots indicate direction and relative magnitude of vertical shear over $0 < z < 2.5$ km. Contours of q_r are multiplied by 10^{-4} in panels a-f. Precipitation contours in mm; topographic contours in intervals of 250 m.

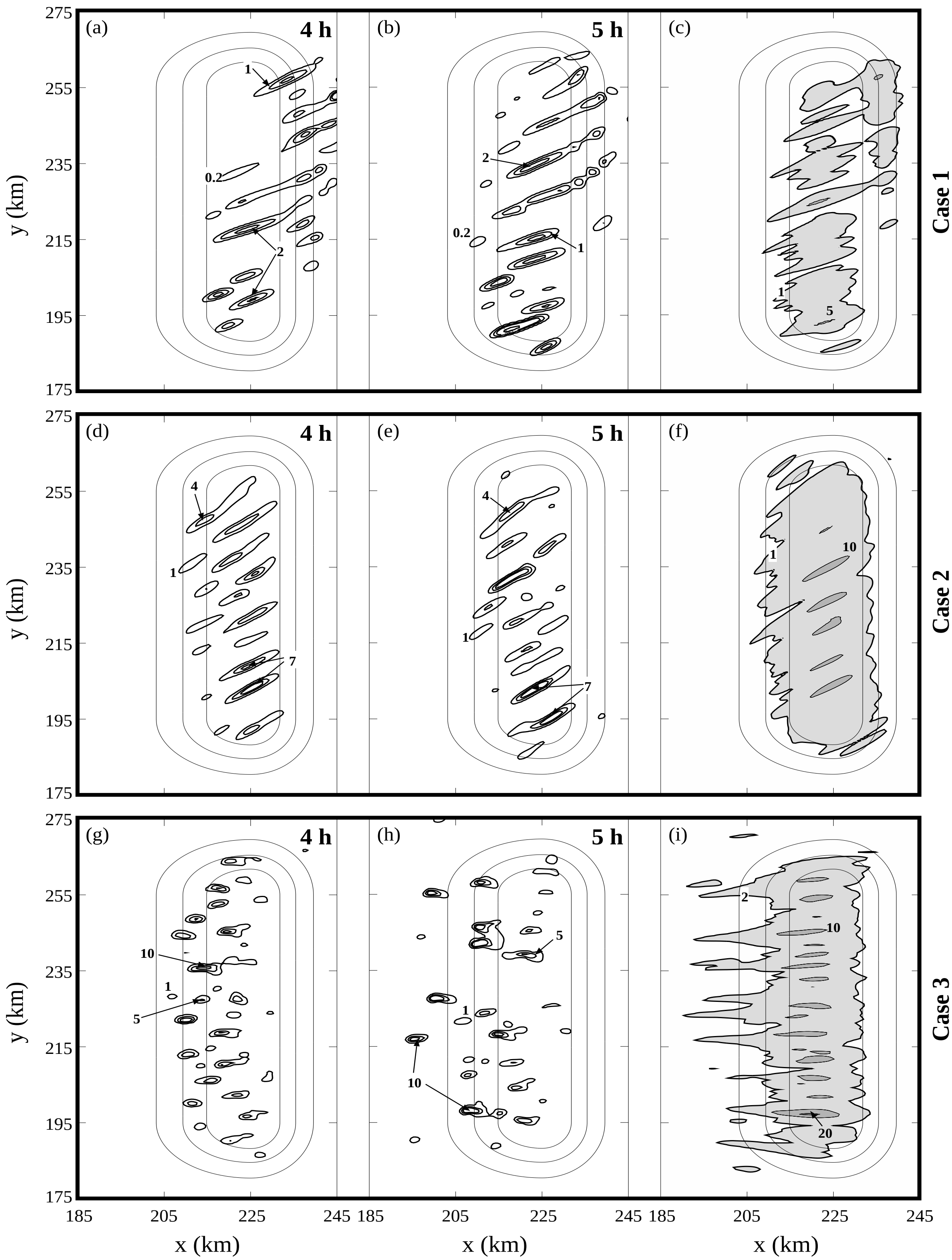

FIG. 8: As in Fig. 7, except that the topography does not contain small-scale random noise.

While prominent isolated peaks may in some cases profoundly influence the cumulative precipitation over the mountainous terrain, even the much smaller-scale randomized roughness elements in the simulations of section 4 were sufficient to anchor many of the rainbands in Cases 1 and 2 to specific locations and greatly increase the maximum precipitation accumulations over the corresponding smooth-topography simulations. To determine how closely these quasi-stationary bands are tied to the underlying pattern of random topographic noise, we first construct a new topographic noise field that is moderately smoother than those of section 4 by passing the noise an additional eight times through the aforementioned two-dimensional diffusion operator, then re-scaling the perturbations to 30 m rms amplitude. This allows the roughness elements to be more clearly distinguished by the eye, as may be seen by comparing 30 m contours of positive terrain perturbations between the original Case-2 simulation (Fig. 9a) and a simulation that is identical except for the use of this smoothed topographic noise field (Fig. 9b). Despite the obvious differences in the topographic noise, the cumulative rainfall patterns are nearly identical between the two simulations. For example, the most intense bands A and B undergo very little modification as the topography is smoothed, indicating that the very fine-scale roughness of the underlying topography does not have a large impact on the overall solution. Further investigation is necessary to determine whether this invariance of band properties over roughened topographies with different levels of smoothing is a physically meaningful result. Very fine-scale roughness may excite modes that cannot be adequately resolved in our simulations, thus limiting the sensitivity of the orographic rainbands to these topographic features.

Figures Fig. 9b and 9c illustrate how the location of individual bands change in response to a southward shift in the pattern of the smoothed small-scale roughness elements. Without altering the position of the larger-scale ridge between these two simulations, the small-scale roughness field is shifted 2 km to the south in the simulation shown in Fig. 9c. A shift of slightly less than one-half wavelength was chosen because it minimizes the differences in the flow impinging on the individual roughness elements that would accompany large along-ridge displacements due to the systematic variations in low-level winds produced by the larger-scale ridge. Almost all of the bands in Fig. 9c are shifted 2 km south of their position in Fig. 9b with only minimal changes in their size and intensity. Note in particular that the strong bands A and B very accurately maintain their position with respect to the underlying roughness field as that field is shifted to the south.

The strong influence of low-amplitude topographic irregularities on the location of orographic rainbands as revealed by the preceding comparison may help to explain the behavior of observed bands such as B3 in Fig. 2b and B6 in Figs. 2c and 2d, which persisted in quasi-stationary locations despite the lack of obvious small-scale topographic peaks in their immediate vicinity. Like the simulated bands in Figs. 7 and 9, these observed bands may have been fixed to small-scale features with amplitudes of less than 100 m, which are not clearly apparent in the topographic contours of Fig. 2. Further investigation is necessary to determine the physical mechanism by which these small-scale obstacles are so effective at fixing the location of orographic rainbands.

6. Atmospheric influence upon convective structure

While small-scale topographic features tend to increase the organization and steadiness of those orographic rainbands that develop in a given event, atmospheric properties appear to determine whether rainbands are preferred over more cellular structures as the primary mode of convective organizaton. Two such properties considered in this section are the vertical shear and the low-level stability of the upstream flow.

6.1 *Vertical wind shear*

Numerous theoretical investigations (e.g., Asai 1972, Sun 1978) have found that longitudinal bands aligned with the environmental shear vector are the preferred mode of convection for small-amplitude perturbations over flat terrain in both dry and saturated atmospheres. Such shear-parallel convection has been observed in numerous studies, among them investigations of cloud streets (Malkus 1962) and tropical rainbands (Hildebrand 1997). Convective bands aligned with the shear (and mean wind) vector also were seen to develop in the numerical simulations of shallow orographic convection in Kirshbaum and Durran (2003), suggesting that this mechanism may also organize convection over mountainous topography.

To determine the influence of vertical shear on the organization of the convective features in the quasi-idealized simulations of section 4, vertical profiles of U and V over $0 < z < 2.5$ km, the approximate layer in which the orographic clouds reside, are compared in Fig. 10 at $x = y = 185$ km and $t = 4$ h. These profiles have been extracted after the flow has become quasi-steady to reflect the modifications to the far upstream velocity profiles (Figs. 5c and 5d) caused by the increased surface friction and boundary layer depth over land. Because the velocity is reduced to nearly zero magnitude at the surface, the directions of the mean wind and the vertical shear are essentially identical within this layer. The relationship between shear direction and rainband orientation is shown by plotting the $0 - 2.5$ km mean shear vectors on each of the q_r plots in Fig. 7. In all three cases, the rainbands are roughly parallel to the shear vectors across the convective layer. Note that the vertical shears in Cases 1 and 2 are greater than in

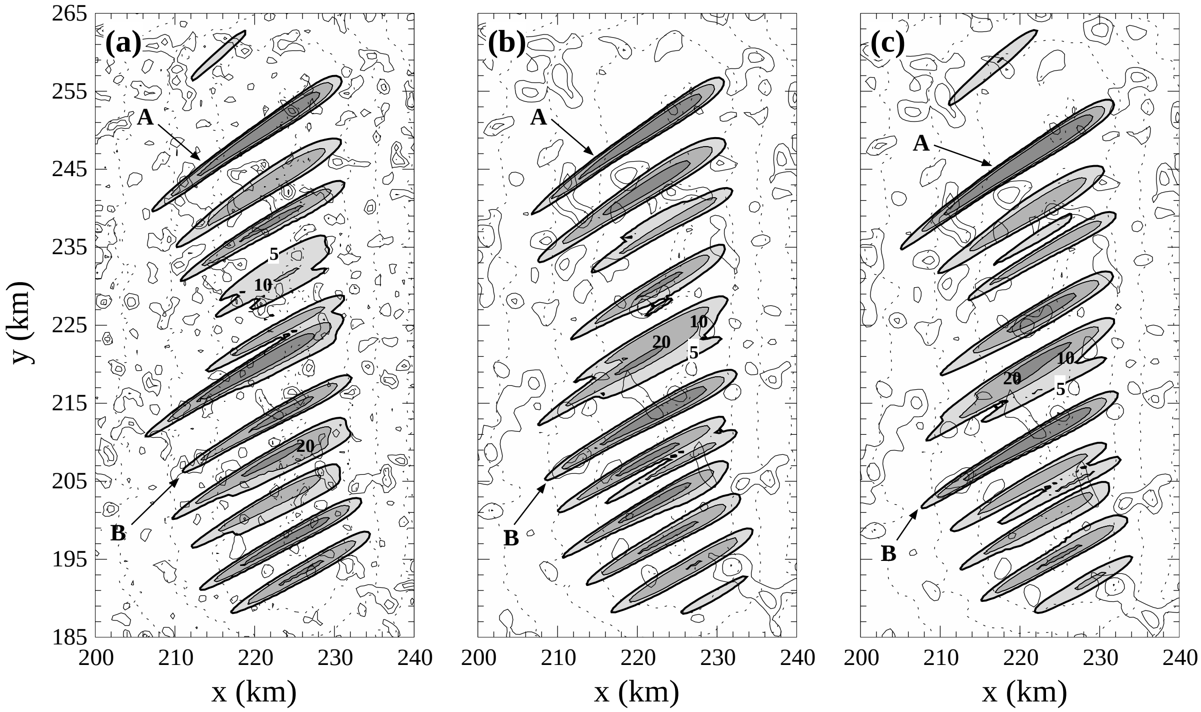

FIG. 9: Cumulative precipitation fields of simulations of Case 2 at $t = 5$ h with different topographic roughness fields. (a) Roughened field obtained by four passes through diffusion operator (same as Fig. 7f with different contour interval), (b) smoothed field passed eight additional times through diffusion operator, (c) same as (b), with noise field shifted 2 km to the south. Precipitation contours are in mm; contours of underlying topography at 250 m intervals shown by dashed line; positive perturbations in topographic noise field given by solid lines at 30 m contour intervals.

Case 3; these stronger shears may serve to enhance the banded structure of the convection.

6.2 *Low-level stability*

From both the radar images and the simulation results, two obvious differences between Case 3 and the other cases are apparent: convective cells in Case 3 form upstream of the mountain, and those rainbands that do occur over the mountain are far less prevalent and organized. These two differences appear to be related, because when convective cells initiate upstream and drift over the mountain, they disrupt the organization of convective circulations that might otherwise form over the orography.

In order for moist convective cells to develop upstream of the cap cloud, some nonorographic source of upward motion is required to bring air parcels to their level of free convection (LFC). This ascent might be produced by small-scale eddies initiated by thermal or mechanical perturbations in the planetary boundary layer. As described in section 4, such perturbations are represented in our simulations by a random initial field of thermal noise that is continually replenished at the upstream boundaries of the finest numerical grid. These buoyancy perturbations force dynamical responses that vary greatly depending on the static stability within the layer. For example, thermal perturbations in unstable layers yield amplifying circulations that can rapidly lift moist parcels to saturation and their LFC, while in strongly stable layers the majority of perturbation energy is radiated away by gravity waves. Thermal perturbations may also generate moist convection in weakly stable layers with high moisture content and low convective inhibition (CIN), where the reduced resistance to vertical ascent may allow sufficiently buoyant parcels to reach their LFC.

Let us therefore compare the static stability [defined as $N^2 = gd\ln\theta_v/dz$, where $\theta_v = \theta(1+0.61q_v)$], relative humidity, and CIN[2] over $0 < z < 1$ km in Figs. 11a, 11b, and 11c, respectively. As indicated in Fig. 11, the combination of comparatively low static stability below 0.5 km—and high relative humidity above—makes the CIN for Case 3 much lower than that in the other cases. As a result of the weak stability and low CIN,

[2]Defined as $g\int_z^{LFC}\left[(T_v(z'))_p - (T_v(z'))_e/(T_v(z'))_e\right]\,dz'$, where $(T_v)_p$ and $(T_v)_e$ are the virtual temperatures of the displaced parcel and background environment, respectively. Note that CIN, which is usually defined as a single value corresponding to the surface, is calculated pointwise over the entire layer.

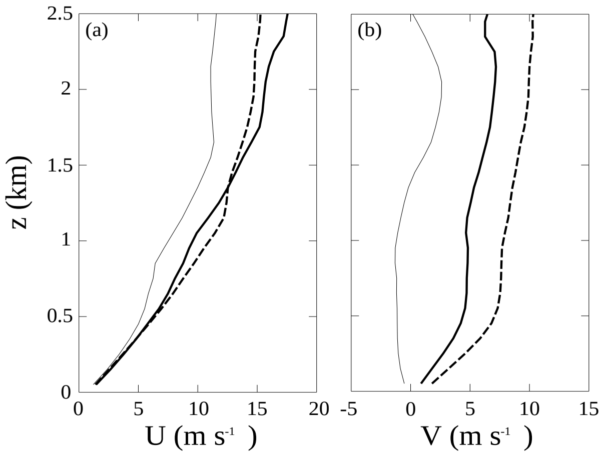

FIG. 10: Velocity profiles over $0 < z < 2.5$ km for Cases 1, 2, and 3: (a) U, (b) V. Case 1 given by thick solid line, Case 2 by thick dashed line, and Case 3 by thin solid line.

parcels rising from low levels in Case 3 can reach their LFC comparatively easily, which appears to explain the presence of convective cells upstream of the mountain in both the observations and simulations of this event. In addition to controlling the strength of vertical motions of flow-based perturbations, the low-level stability upstream of the mountain may also directly affect the preferred structure of formations that occur within the orographic cap cloud. The nature of this relationship is a topic of continued investigation.

7. Conclusions

Three cases of banded precipitation over the Oregon Coastal Range have been examined through both observations and numerical simulations. NEXRAD radar reflectivity imagery indicated well-defined rainbands on 9-10 April 2002 (Case 1) and 12-13 November 2002 (Case 2), with less organized precipitating structures on 12 October 2003 (Case 3). The steady nature of the banded formations in Case 2 produced high small-scale variability in precipitation accumulation, with two rain gauges within the mountains recording a 65 mm difference in precipitation over the seven-hour event despite being located only 20 km apart. Although the highest radar reflectivities were seen in Case 3, the more disorganized convection during that event did not produce the large localized precipitation accumulations seen in Case 2. Case 1 was characterized by cellular features at early times, followed by the formation of organized bands with smaller horizontal scales and weaker reflectivities than those in Case 2. Some of the observed rainbands preferentially formed over and downstream of isolated peaks on the elevated terrain, but others could not be clearly tied to small-scale topographic obstacles.

The precipitating structures apparent in the radar data—and the observed differences in convective behavior between the three cases—were qualitatively reproduced in quasi-idealized simulations of these events. The Case-2 simulation produced the most robust and steady rainbands with the greatest cumulative precipitation. The bands in the Case-1 simulation were weaker and less steady, producing far less precipitation. As in the radar data, both cellular and short banded features of significant intensity were apparent in the Case-3 simulation, but these produced smaller maximum rainfall accumulations than in Case 2 because the precipitating structures were not as stationary.

Small-scale topographic roughness was found to modestly increase the organization—and greatly increase the steadiness—of convective rainbands in comparison to otherwise identical simulations for flow over a completely smooth mountain. As a result, the cumulative surface precipitation in the roughened topography simulations was far greater in the more banded events (Cases 1 and 2). Orographic rainbands with similar scales and locations as the roughened-topography Case-2 simulation still developed over the mountain when the small-scale noise field in the Case-2 simulation was made smoother, suggesting that the bands were not sensitive to the very short-wavelength roughness elements on the topography. Nevertheless, the strong influence of small-scale topography on the location of orographic rainbands was demonstrated as the bands shifted southward in phase with a southward shift in the topographic noise pattern.

Consistent with the results of Cosma et al (2002), larger sub-range-scale peaks were also shown to significantly influence the location of the rainbands. In particular, the addition of a 500 m bump 30 km upstream of the mountain peak tripled the cumulative precipitation downstream of the bump with respect to that in the corresonding bump-free simulation. By contrast,

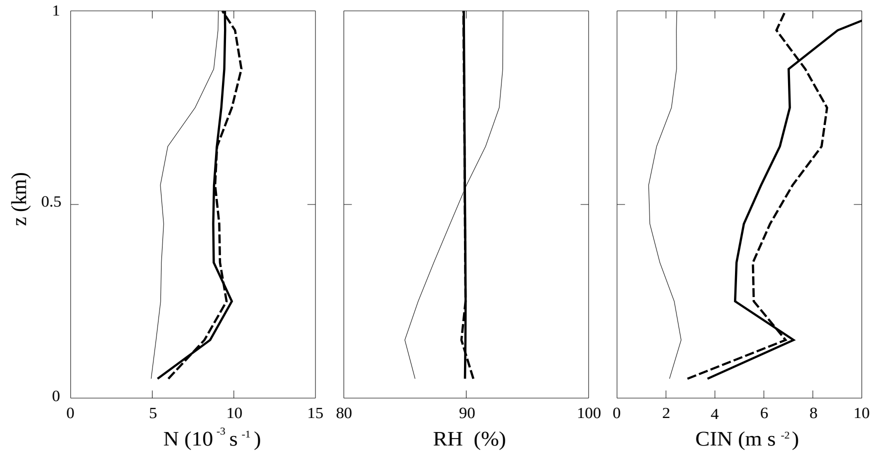

FIG. 11: Low-level thermodynamic profiles for Cases 1, 2, and 3: (a) N, (b) relative humidity, and (c) CIN. Case 1 given by thick solid line, Case 2 by thick dashed line, and Case 3 by thin solid line.

no significant increases in the accumulated surface precipitation were found when an identical bump was shifted 15 km closer to the mountain crest, indicating the considerable sensitivity of rainband formation to the location of the isolated peaks.

The organization of shallow orographic convection appears to be influenced by vertical wind shear and the stability of the upstream thermodynamic profile. Cases 1 and 2 had the greatest low-level shears and the most organized shear-parallel rainbands. Case 3, in addition to having the weakest low-level shear, had the weakest low-level stability and the lowest CIN; this thermodynamic structure favored the development of convective cells upstream of the mountain. As these cells drifted downstream, they dominated the precipitation pattern and tended to disrupt the organization of any rainbands that otherwise might have developed over the mountain. Elongated orographic rainbands were more favored in Cases 1 and 2, which had relatively stable low-level thermodynamic profiles that inhibited convective development upstream of the cap cloud. Further investigation is warranted to learn more about the atmospheric parameters controlling the preferred convective structures in shallow orographic precipitation events.

References

Anquetin, S., Minsicloux, F., Creutin, J.D., Cosma, S., 2003: Numerical simulation of orographic rainbands.*J. Geophys. Res.-Atmos.*, **108 (D8)**, Art. No. 8386.

Caraceña, F., R.A. Maddox, L.R. Hoxit and C.F. Chappell, 1979: Mesoanalysis of Big Thompson storm. *Mon. Wea. Rev.* **107**, 1-17.

Chapman, D., and K.A. Browning, 1999: Release of potential shearing instability in warm frontal zones. *Quart. J. Roy. Meteor. Soc.*, **125**, 2265-2289.

Chu, C.-M., and Y.-L. Lin, 2000: Effects of Orography on the Generation and Propagation of Mesoscale Convective Systems in a Two-Dimensional Conditionally Unstable Flow. *J. Atmos. Sci.* **57**, 3817-3837.

Cosma, S., Richard, E., and Miniscloux, F., 2002: The role of small-scale orographic features in the spatial distribution of precipitation. *Quart. J. Roy. Meteor. Soc*, **128**, 75-92.

Durran, D.R., and J.B. Klemp, 1983: A compressible model for the simulation of moist mountain waves. *Mon. Wea. Rev.* **111**, 2341-2361.

Epifanio, C.C., and D.R. Durran, 2001: Three-dimensional effects in high-drag-state flows over long ridges. *J. Atmos. Sci.* **58**, 1051-1065.

Hobbs, P.V., R.C. Easter, and A.B. Fraser, 1973: A theoretical study of the flow of air and fallout of solid precipitation over mountainous terrain: Part II. Microphysics. *J. Atmos. Sci.* **30**, 813-823.

Houze, R.A., and S. Medina, 2003: Orographic enhancement of precipitation in midlatitudes: results from MAP and IMPROVE II. *Int. Conf. on Alpine Meteor. (ICAM) and the Meso. Alpine Prog. (MAP)*, Brig, Switzerland.

Jiang, Q., 2003: Moist dynamics and orographic precipitation. *Tellus*, **55A**, 301-316.

Kirshbaum, D.J., and D.R. Durran, 2004^1: Factors governing cellular convection in orographic precipitation. *J. Atmos. Sci.*, **61**, 682-698.

Kirshbaum, D.J., and D.R. Durran, 2004^2: Observations and modeling of banded orographic convection, submitted to *J. Atmos. Sci.* on 17 Mar. 2004.

Miniscloux, F., J.D. Creutin, and S. Anquetin, 2001: Geostatistical analysis of orographic rainbands. *J. Appl. Meteor.*, **40**, 1835-1854.